Progress in Additive Manufacturing
https://doi.org/10.1007/s40964-025-01279-y

RESEARCH

Microstructural assessment of additive-manufactured Inconel 718 samples subjected to heat treatments for enhanced mechanical properties

Thiago Roberto Felisardo Cavalcante[1] · Douglas Giovanni Bon[1] · Fábio Edson Mariani[1] · Reginaldo Teixeira Coelho[1] · Jairo Alberto Muñoz[2] · Jessica Calvo Muñoz[2] · Giovani Gonçalves Ribamar[3,4] · João Pedro Oliveira[3] · António Manuel de Bastos Pereira[4] · Julian Arnaldo Avila Diaz[5]

Received: 6 May 2025 / Accepted: 27 July 2025

Abstract

Directed energy deposition (DED), a laser additive manufacturing (AM) process, has attracted a significant attention as a potential alternative to conventional manufacturing methods, due to its high deposition efficiency, flexibility, and precision. Despite these advantages, components produced by DED often face critical challenges, including residual stresses, microsegregation, and the formation of non-equilibrium phases due to rapid cooling during the AM process. These issues are particularly critical for Ni-based superalloys such as Inconel 718 (IN718), widely used in the aerospace, energy, and marine industries for their excellent high-temperature strength and corrosion resistance. The mechanical performance of IN718 primarily depends on precipitation hardening via γ' and γ'' phases. In contrast, the formation of deleterious phases, such as δ and Laves, can severely impair performance by depleting key alloying elements and increasing brittleness. Thus, heat treatments (HTs) are vital in addressing these challenges by reducing microsegregation, homogenizing elemental distribution, and promoting the precipitation of strengthening phases. Therefore, this study investigates the effects of six distinct heat-treatment routes on the microstructural evolution, hardness, tensile properties, and fracture behavior of DED IN718 samples. The relationship between microstructure and mechanical responses is analyzed and compared to a forged IN718 counterpart. The results offer valuable insights for optimizing heat-treatment strategies to improve the structural integrity and mechanical reliability of DED-fabricated IN718 components.

Graphical abstract

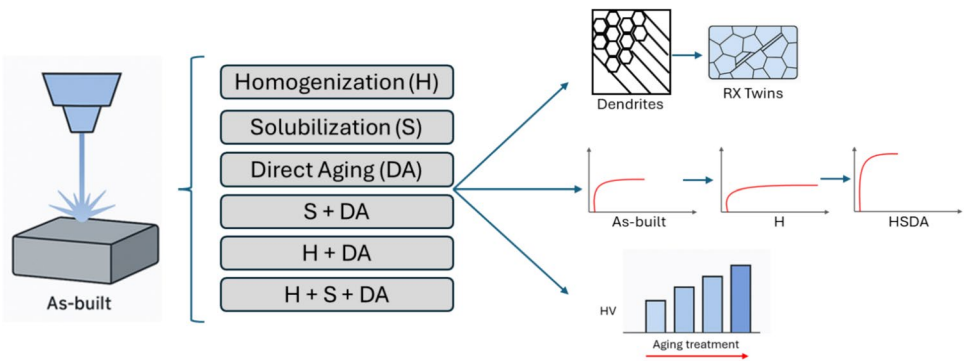

Keywords IN718 · Heat treatment · Microstructure · Additive manufacturing · Mechanical properties

Extended author information available on the last page of the article

Published online: 05 August 2025

1 Introduction

Recently, laser additive manufacturing (AM) techniques have been extensively researched and are in a state where they could be considered potential candidates to replace traditional manufacturing methods when needed [1]. Laser beam directed energy deposition (DED) is a type of AM that deposits thin layers of metal powder and melts them using a high-energy laser beam; furthermore, it can deposit metallic materials and functional coatings. DED has the advantages of high deposition efficiency, flexibility, and precision [2]. However, due to the rapid cooling of the process, residual stresses, microsegregation, and the formation of non-equilibrium phases are a common feature in as-built components [3].

Ni-based superalloys, such as Inconel 718 (IN718), are heat-treatable, hot corrosion resistant, and preferred for the fabrication of aerospace engines, turbine blades, injectors, and many other high temperatures and/or high-pressure components [2, 4]. This alloy, specifically, is mainly strengthened by precipitation hardening, via the precipitation of γ' and γ'' phases [5]. Moreover, the solid solution hardening effects of some elements in the γ matrix, such as Nb and Mo, can be additional factors to improve the mechanical properties. The presence of micro/nano-sized γ' and γ'' phases control the mechanical properties of the IN718 alloy. On the other hand, deleterious phases, such as δ and Laves phases, can degrade the materials' properties, either due to the incoherent nature of the phase within the matrix, or the inhibition of γ' or γ'' precipitation [6].

The microsegregation of elements and the presence of deleterious phases, typical in AM components, make the elemental distribution uneven, which also impacts the precipitation of γ' and γ'' phases [7]. Laves phase forms in the interdendritic regions and is known to deteriorate mechanical properties, such as strength, ductility, fatigue, and creep, since it depletes essential precipitation elements, besides facilitating crack initiation and propagation due to its brittle nature [7, 8]. Applying heat treatments (HT) and controlling the solidification conditions during the deposition are two ways to reduce the microsegregation and formation of the Laves phase. It has been reported that Nb segregation and Laves phase formation can be reduced by increasing the cooling rate from the liquid material [9]. However, controlling the solidification conditions is rarely achievable due to the complicated solidification of the AM processes [8]. As such, post-fabrication HTs are vital to achieve excellent mechanical performance and meet service requirements through the elemental distribution homogenization and precipitation of the strengthening phases [10].

The precipitation hardening HT involves the dissolution of the Laves phase, since it releases Nb and Ti back to the matrix [11]. Generally, a two-step direct aging (DA) and solubilization (S) are performed, and, in some cases, a homogenization step is also applied. The solubilization typically occurs in the range of 950–1100 °C to dissolve the Laves phase and release Nb and Ti into the matrix; direct aging usually ranges from 600 to 800 °C and results in the formation of γ' and γ'' precipitates. Furthermore, homogenization HTs (H) can also eliminate Laves and microsegregation, enhancing the homogeneous precipitation of strengthening phases [12].

Several studies have been conducted regarding the influence of HTs on AM IN718. Qi et al. [12] reported that the microstructure and tensile properties of IN718 manufactured by DED with DA achieved high tensile strength values with low ductility. Huang et al. [13] showed that, for alloys fabricated via PBF-LB process, different solution treatment temperatures, ranging from 980 to 1280 °C for 1 h, implied different Laves phase dissolution degrees. Burad et al. [7] investigated the effect of S and S + DA HTs and concluded that solution treatment at 980 °C, to dissolve the Laves phase and microsegregation spots, led to a good precipitation quality. Zhai et al. [14] found that a simple aging process could precipitate an amount of γ' and γ'' phases capable of enhancing the mechanical properties of IN718, with weak microsegregation and fine Laves phase still present. However, it could not change the typical columnar dendrite structure. Zhao et al. [15] demonstrated that a homogenization temperature of 1180 °C can eliminate residual stress and promote recrystallization of IN718 manufactured by LB-PBF. Regarding the Laves phase, Sui et al. have studied its dissolution [16], who investigated the effect of a 1050 °C solubilization with DA on DED IN718 samples, showing a large improvement in high-temperature mechanical behavior. Xu et al. [10] studied the microstructural evolution and the mechanical performance of AMed IN718 under three HTs: DA, S + DA, and H + S + DA, and concluded that different as-built microstructures require different HTs; a similar study was also performed by Yu et al. [17], who focused on the fracture behavior of the DED IN718 deposited material. Furthermore, as-built microstructures, according to Jang et al. [18], studied the precipitation kinetics of secondary phases formed by the heat accumulation during the IN718 DED deposition.

This study investigates the effects of six different heat-treatment strategies on microstructural evolution, hardness, tensile properties, and fracture behavior of IN718 samples produced by DED. Special focus is placed on the influence of these treatments on the precipitation of strengthening phases and the dissolution of deleterious phases such as the Laves phase. The mechanical performance of the treated AMed samples is critically analyzed to assess the effectiveness of post-processing in mitigating typical additive manufacturing defects and performance. The findings aim to

support better heat-treatment routes for AMed IN718 alloys, promoting improved structural integrity and mechanical reliability for high-performance applications.

2 Experimental procedure

2.1 Materials

For this study, gas-atomized IN718 powder with an average size of 93 µm, produced by Carpenter Additive Inc., was used. Its morphology can be seen in Fig. 1. The powder's chemical composition, expressed in weight percentage (wt.%), was as follows: Ni 52.30, Cr 19.72, Nb + Ta 4.96, Mo 3.30, Co 0.53, Ti 0.39, Si 0.09, Mn 0.04, C 0.01, P 0.01, with Fe in balance.

2.2 Materials processing

The depositions were conducted on AISI 1020 steel with a thickness of 5 mm, which was end-milled and cleaned before the experiments. A BeAM Inc. Modulo 250 5-axis Directed Energy Deposition-Laser Beam (DED) system was utilized, equipped with a 1 kW continuous-wave ytterbium fiber laser (Model YLR-1000-MM-WC-Y14, IPG Photonics Inc.), operating at a wavelength of 1070 nm and a focused spot size of 0.8 mm. The laser was mounted on a coaxial deposition head, and the system incorporated a dual-powder feeder for material deposition. The parameters utilized for this work were a laser power of 500 W, a crosshead speed of 2000 mm/min, a feed rate of 5 g/min, and 90° rotation between layers. These parameters were determined in a previous study, which evaluated various combinations of power, scanning speed, and powder feed rate to achieve high-integrity single tracks [19].

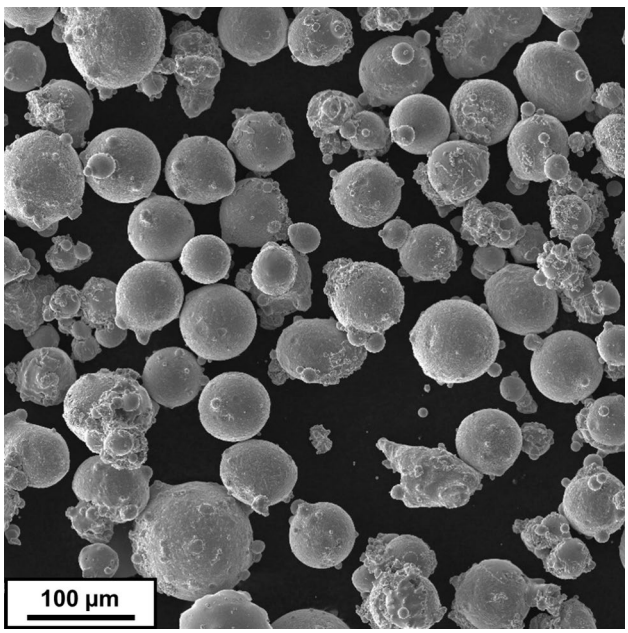

Fig. 1 Morphology of IN718 powder, as analyzed by SEM

All heat treatments (HT) were carried out in a Jungbrand muffle furnace (LF07013 model). The six HT routes employed in this study were designed to evaluate the effects of homogenization, solubilization, and aging on the microstructure and mechanical properties of the material. The different kinds of heat treatments used are: (i) homogenization (H), consisted of heating the samples to 1100 °C for 1.5 h, followed by water quenching; (ii) solubilization (S), where the material is isothermally heat-treated at 1000 °C for 1.0 h, also followed by water quenching; and (iii) direct aging (DA), consisted on an aging at 720 °C for 8 h, followed by controlled cooling at 50 °C/h down to 620 °C, where the samples were held for an additional 8 h, and then air-cooled to room temperature. In addition to these isolated heat treatments, three combinations were also evaluated: homogenization followed by direct aging (HDA), solubilization followed by direct aging (SDA), and homogenization followed by solubilization and direct aging (HSDA).

To assess the porosity level after manufacturing, a Bruker Skyscan 1272 microtomograph was utilized. It features an 11 MP detector (4032 × 2688 pixels) and operates at 10 W. The sample, measuring 2 mm × 3 mm × 8 mm, was scanned at a resolution of 2 µm with a step size of 0.3°. The 3D model was reconstructed and rendered using the Dragonfly™ 2022.2 software developed by Comet Group. Volumetric porosity was then calculated by applying color thresholding to distinguish between the pores and the solid material.

2.3 Microstructural characterization

The samples underwent standard preparation for metallographic evaluation, involving abrasive cutting, manual grinding with sandpapers, and sequential surface polishing using 1.00 and 0.25 µm diamond suspensions. Final etching was done using waterless Kalling's reagent (100 ml ethanol, 100 ml HCl, 5 g $CuCl_2$) to reveal the microstructure. Cross-sectional microstructure observations were conducted with an Olympus LEXT 4100 3D laser microscope and an FEI® FE-50 Scanning Electron Microscope (SEM). Microhardness was assessed using a Buehler Model 1600 6300 tester by ASTM E384 [20], employing a 0.5 N load for 15 s, Fig. 2d.

Further microstructural details were examined via EBSD using a Quanta 650 FEG-SEM and high-speed acquisition EBSD system. Data were analyzed in TSL OIM and MTEX, with EBSD scans performed over 2000 µm × 1500 µm (step size 1.5 µm) and 500 µm × 500 µm (step size 0.5 µm). Maps achieved ≥ 90% indexing; non-indexed points were

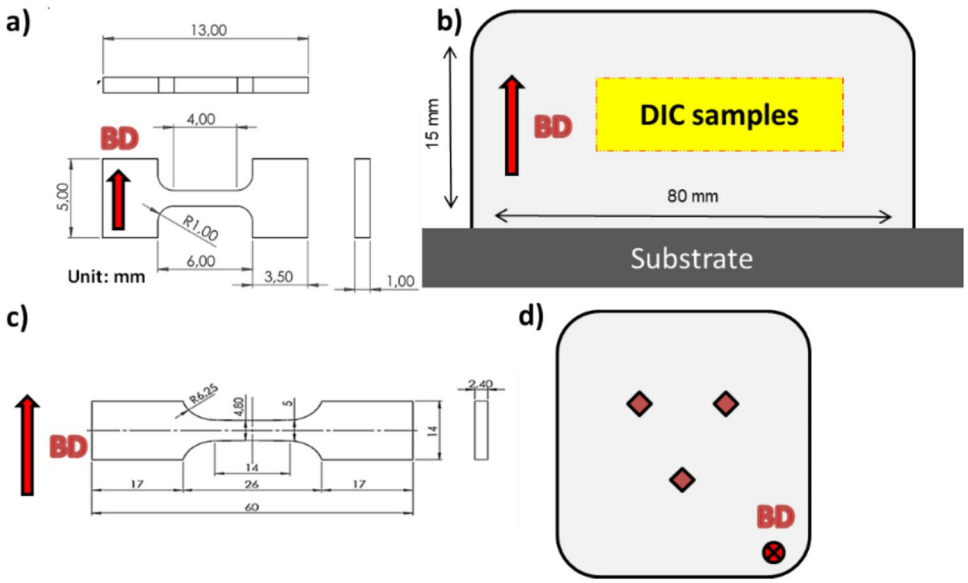

Fig. 2 **a** DIC test specimen geometry, **b** deposited block for mechanical testing, **c** standard tensile test specimen geometry, and **d** schematic for the hardness tests

corrected using the grain dilation correction method, while grains with less than 2 pixels were excluded. GND densities were obtained via the Kernel Average Misorientation (KAM) and the Weighted Burgers Vector (WBV) [21] approaches. Boundaries were classified by misorientation: > 15° (high-angle grain boundaries—HAGB), 5–15° (low-angle grain boundaries—LAGB), and 2–5° (subgrain boundaries—SGB).

Synchrotron energy-dispersive X-ray diffraction (EDXRD) was carried out at P61 High Energy wiggler beamline/LVP, installed at Petra III, Hamburg, Germany. Transmission-mode scans employed 10 wigglers (30–200 keV range), with spectra collected along 10 mm line scans at 0.2 mm steps. Two HPGe detectors positioned at $2\theta Ch0 = 7.557°$ and $2\theta Ch1 = 7.594°$ captured data from a $0.1 \times 0.1 \times \approx 3$ mm^2 gauge volume. Exposure time per spectrum was 1 s. Raw data were processed using the in-house Python scripts.

2.4 Mechanical testing

Digital Image Correlation (DIC) tensile testing was performed using a Deben Microtest Tensile Stage on dog-bone samples (gauge length: 4 mm × 1 mm × 1 mm) at 0.4 mm/min (Fig. 2a and b). Load, displacement, and axial strain were captured via a Balser camera (2048 × 2048 pixels at 75 fps) using 35-, 50-, and 75-mm lenses. DIC analyses were done using an open-source DIC package (Ncorr) [22] to generate strain maps and profiles. Conventional tensile tests followed ASTM E8-24 [23], performed under displacement control (1 mm/min) on a 100 kN MTS Landmark N servo-hydraulic system. Specimens, extracted horizontally, are illustrated in Fig. 2c.

3 Results and discussion

3.1 Microstructural characterization

3.1.1 Microstructure of as-built samples

Figure 3 presents the porosity analysis for the as-built condition, conducted using X-ray diffraction microtomography. This analysis estimated a volumetric porosity of approximately 0.37%, with pore sizes ranging from 13 to 150 µm. The pores exhibited irregular morphologies aligned with the building direction, as evidenced by the different views of the analyzed solid shown in Fig. 3(a). The porosity size calculations resulted in an average pore size of 64 ± 32 µm and a sphericity of 0.6 ± 0.15 for the as-built condition, as illustrated in Fig. 3(b). According to Dass et al. [24], spherical pores (those smaller than 50 µm) and irregularly shaped pores (those larger than 50 µm) are linked to gas entrapment and lack of fusion, respectively. The calculated volumetric porosity of 0.37% falls within the low porosity range and can be achieved under optimal manufacturing conditions in DED. These findings indicate that the processing parameters defined with an energy density of 104 J/mm^3 result in high-quality material.

In our previous study [19], the microstructural analysis of the as-built IN718 samples revealed a predominantly dendritic microstructure, a characteristic commonly observed in additively manufactured components, especially those produced by DED [25]. These structures consist of elongated columnar grains with finer, equiaxed grains in a bimodal manner. This dual morphology is typical of rapid solidification conditions inherent to the process. The dendritic morphology and potential strings of the Laves phase were more pronounced in the interdendritic regions. Additionally,

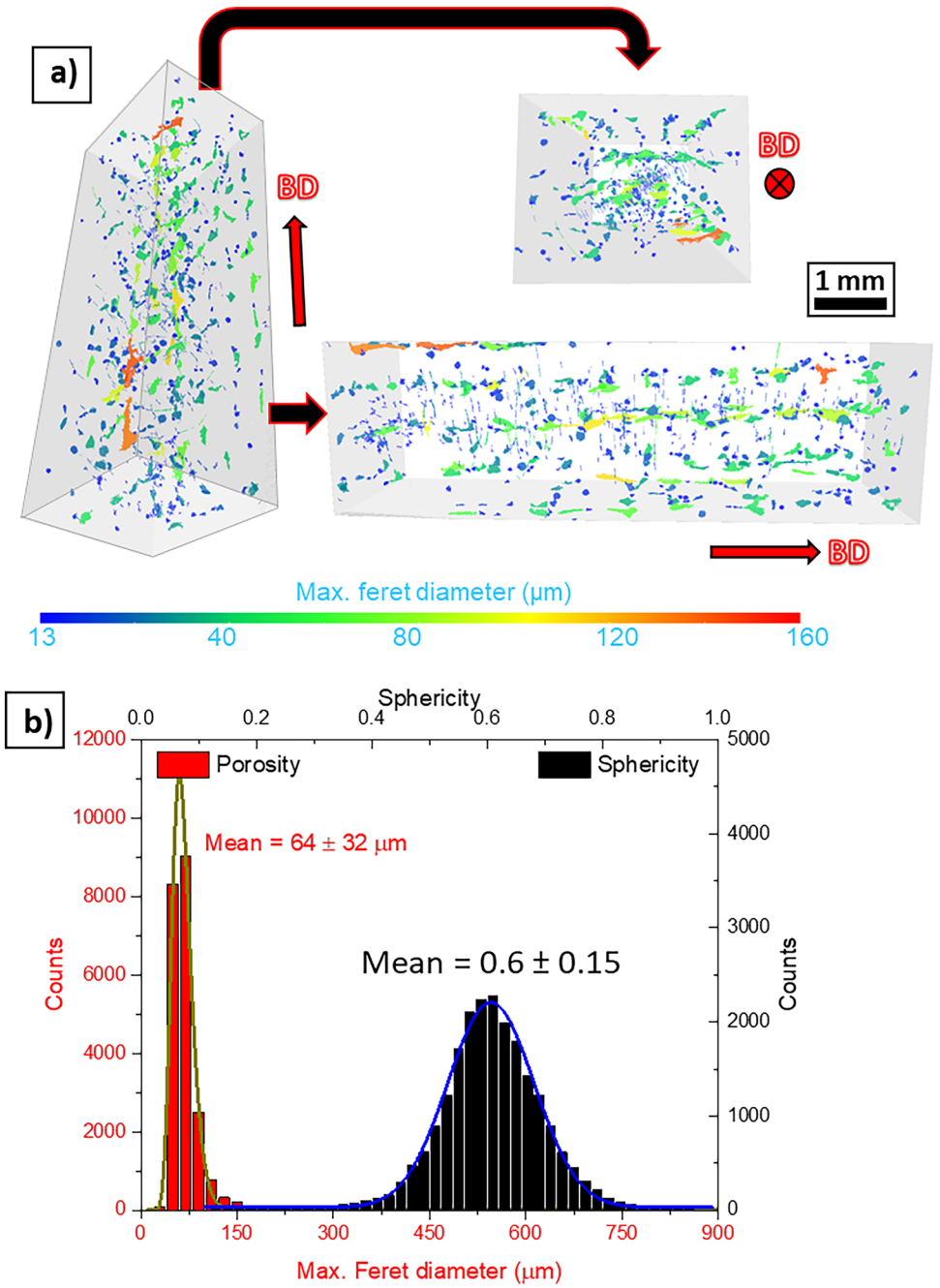

Fig. 3 **a** Porosity distribution in the volume analyzed and **b** porosity and sphericity distributions for the as-built condition

structures resembling δ phase and MC carbides were found, which align with features typically formed due to microsegregation of alloying elements during solidification. These findings are consistent with the literature reports of dendritic cellular structures resulting from fast thermal cycles [26]. The formation of δ and Laves phases, driven by microsegregation, is a well-documented phenomenon in as-built IN718. These phases are detrimental as they deplete the matrix of Nb, an essential element for the precipitation of γ' and γ'', the primary strengthening phases [27]. Furthermore, an as-built sample is analyzed in Fig. 4. The analyzed sample was taken from a small block (15 × 15x15 mm) deposited with a laser power of 500 W and a scan speed of 2500 mm/min, along with a feed rate of 5.2 g/min. Figure 4(a) shows the band contrast map superimposed with grain boundaries as black lines for the as-built microstructure, i.e., before the heat treatments. The red arrow represents the building direction of the sample. It illustrates a microstructure composed of grains with varying morphologies and sizes, ranging from 3 to 200 μm. The grains are predominantly oriented along the building direction, leading to an average grain size of 80 ± 50 μm (see Fig. 4(b)).

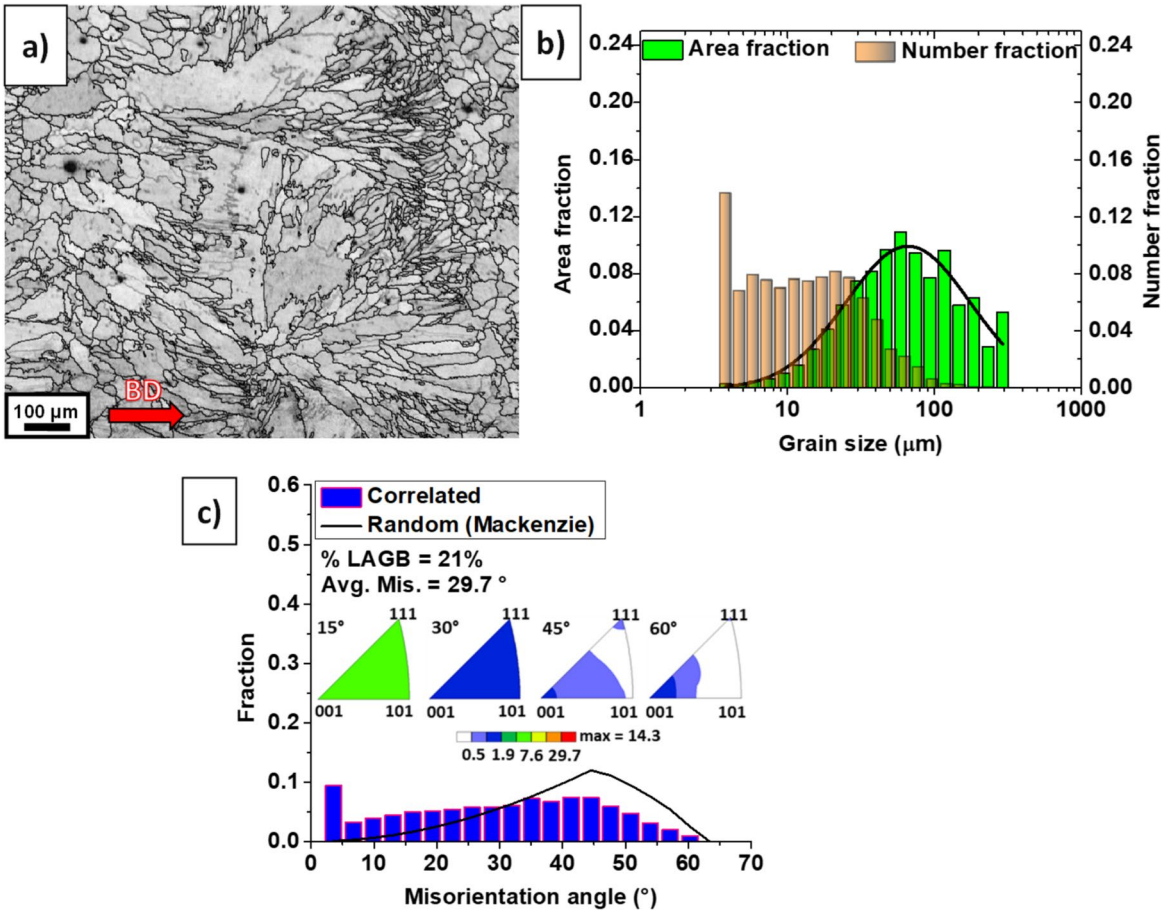

Fig. 4 **a** General view of as-built microstructure, **b** grain size distribution of as-built sample, and **c** misorientation angles of as-built samples

Regarding grain boundary characteristics, the distributions of misorientation angles and axes reveal a random orientation for LAGBs, comprising 21% of the total boundaries. In contrast, HAGBs show a transition toward the ⟨001⟩ direction at misorientation angles greater than 30° (refer to Fig. 4(c)). The significant prevalence of LAGB in the as-built condition is attributed to the high residual stress generated during the manufacturing process. These stresses result in a high density of dislocations caused by the compression and tensile residual stresses within the melt pools [28, 29].

3.1.2 Microstructure of heat-treated samples

EBSD assemblies extracted from the heat-treated samples can be seen in Figs. 5 and 6. It can be seen from Fig. 5a, d, and g that the DA and both solubilized conditions, S and SDA, still present columnar grain morphology, similar to as-built samples. On the other hand, the homogenized conditions, namely H, HDA, and HSDA (Fig. 6a, d, and g, respectively), present annealing twins and recrystallized grains. It can be noticed that the misorientation features change from solubilization and aging only treatments when compared to homogenization treatments, Figs. 5 and 6 b), e), and h). The calculated average misorientations were approximately 30.6°, 28.5°, and 28.2°, with a low-angle grain boundary (LAGB) percentage of 19.5, 28.4, and 32.4% for DA, S, and SDA samples, respectively. When compared to the homogenized counterparts, it can be noticed that the H, HDA, and HSDA present higher values of misorientation angles, 41.3°, 47.4°, and 48.2°, respectively, and lower quantities of LAGBs: 19.0, 7.8, and 9.6% for H, HDA, and HSDA, respectively.

The difference in the average misorientation and percentage of LAGBs can be explained by the recrystallization process promoted by the homogenization treatment. The quantity of LAGBs is generally lower in metallic materials that have undergone recrystallization. This occurs, because recrystallization involves the formation of new deformation-free grains with HAGBs, which replace the deformed structure and the LAGBs present in the material before the process [30]. During recrystallization, the energy stored in the material due to plastic deformation is released by forming new grains. These grains tend to exhibit more random crystallographic orientations, resulting in HAGBs. LAGBs,

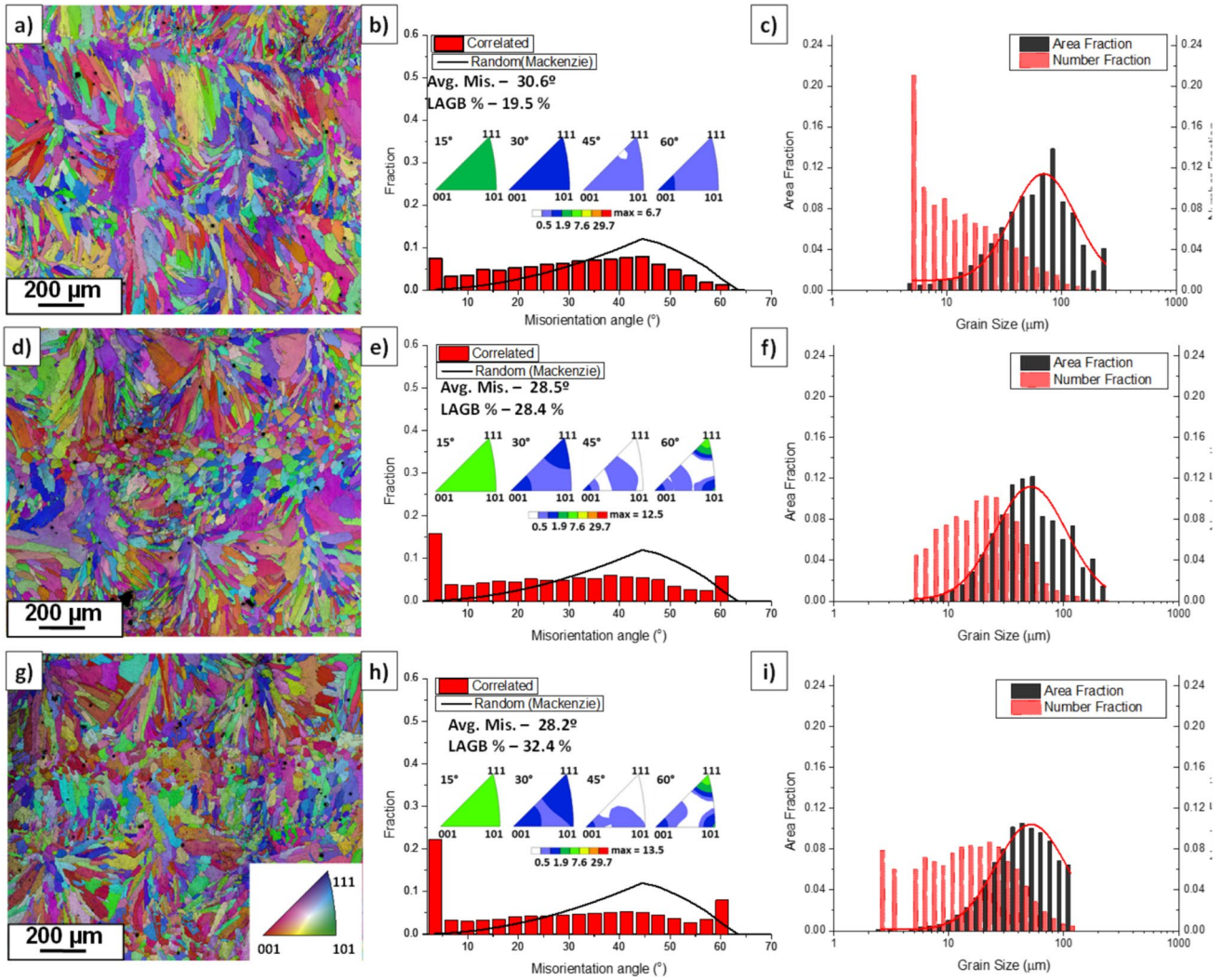

Fig. 5 EBSD results for: DA sample in the first line, S sample in the second line, and SDA condition in the third line. The first column shows the IPF map superimposed with the band contrast map. The second column shows semiquantitative and quantitative misorientation analysis. The third column shows semiquantitative grain area distribution

which are characteristics of substructures within deformed grains, are either eliminated or significantly reduced during this process [30]. This change is evident in the distribution of misorientation axes, where the average misorientation increases for the homogenized materials. This results in a significant shift in the texture of the grain boundaries due to the formation of $\{111\}\langle 111\rangle$ recrystallization twins, which occur at a misorientation of 60°.

The evolution in grain morphology and grain boundary orientation transits from microstructures primarily characterized by low-angle grain boundaries (LAGB) in the solubilized conditions to those dominated by recrystallization twins after the homogenization heat treatment. This remarkable versatility of the alloy in producing a wide range of properties is a testament to its potential to create different mechanical properties. Furthermore, it can be noticed when comparing DA with the other HTs that there is a microtexture change, deviating from the almost random orientation shown by the DA sample to more oriented grain boundaries, as can be seen by the Mackenzie curves in Figs. 5 and 6b, e, and h plots.

From a grain size perspective, the DA, S, and SDA samples exhibit similar characteristics, featuring coarse columnar grain structures. In contrast, the homogenized sample has recrystallized equiaxed and bimodal grains within the observed field, with grain sizes ranging mostly from approximately 10 to 240 µm for the H and HDA samples, with a slight increase in grain size for the HSDA sample, with a grain size ranging from approximately 10 to 290 µm. The observed recrystallization may be associated with the release of residual stresses accumulated during the DED process, as reported in the previous studies for IN718 additively

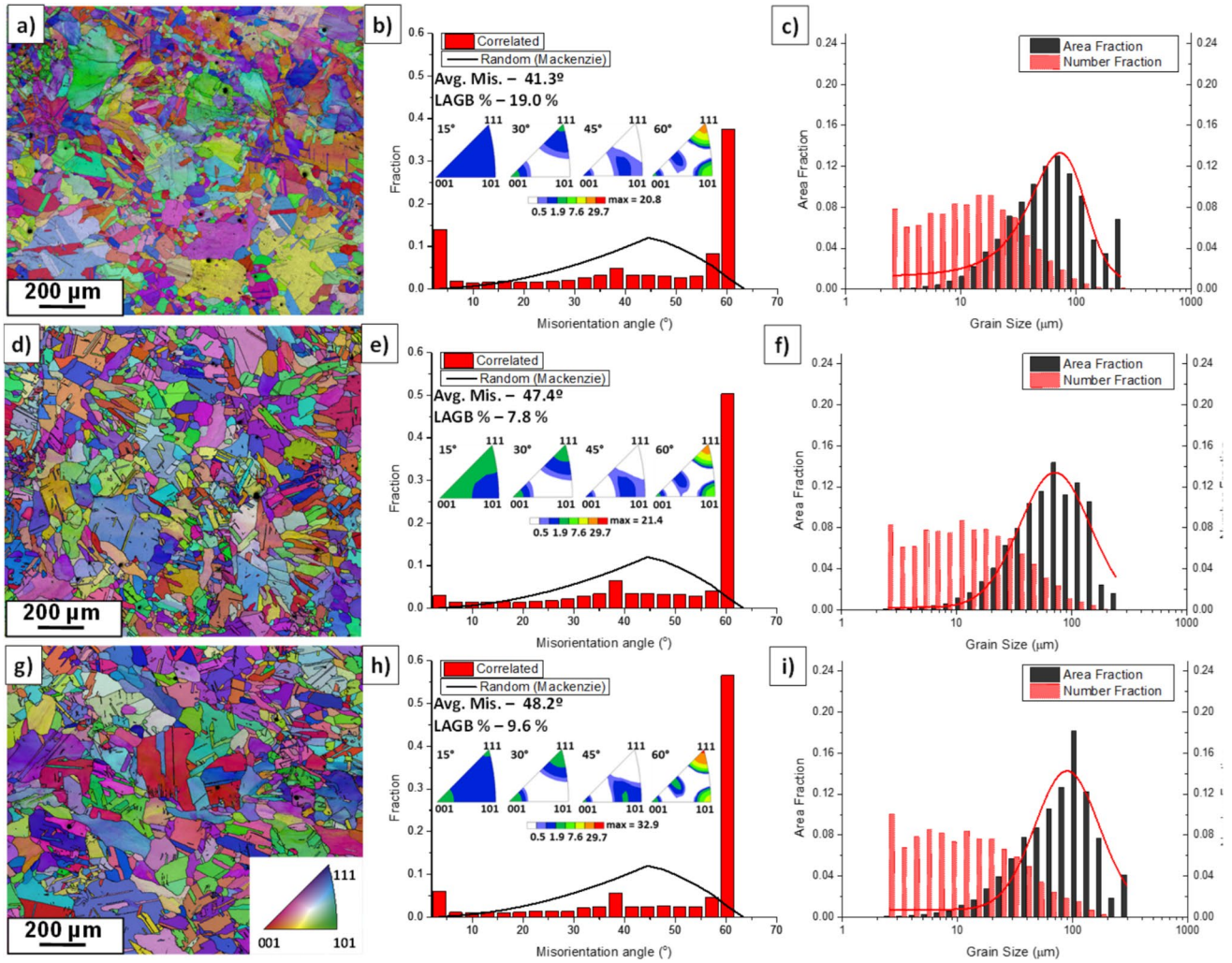

Fig. 6 EBSD results for: H sample in the first line, HDA sample in the second line, and HSDA condition in the third line. The first column shows the IPF map superimposed with band contrast map; the second column shows semiquantitative and quantitative misorientation analysis; the third column shows semiquantitative grain area distribution

manufactured alloys [31, 32]. Although no direct measurement of residual stress was performed in the present work, the microstructural features—such as grain boundary morphology and dislocation rearrangement—suggest that residual stress gradients may have played a role in driving recrystallization during the applied HTs. According to Humphreys et al. [30], the static recrystallization temperature of wrought IN718 is approximately 1020 °C, which is lower than the 1100 °C used in the homogenization treatments of this study. According to the literature, DED processed IN718 exhibits a higher recrystallization temperature than its wrought counterpart, primarily due to the lower residual strain and the high supersaturation of solute atoms in the as-built IN718 produced by DED. In general, wrought IN718 undergoes significant plastic deformation during forging, leading to a considerable accumulation of residual strain energy. As a result, the driving force for recrystallization in wrought IN718 is greater than that in DED-produced IN718, as reported elsewhere [33]. Furthermore, the fast-cooling rates inherent to the DED process significantly enhance the supersaturated solid solubility of alloying elements in the γ matrix, contributing to increased recrystallization temperature [34].

Heat treatments significantly influence the microstructure of this alloy, as reflected in the distribution, orientation, and density of dislocations. Figure 7 displays geometrically necessary dislocations (GND) maps corresponding to the various HTs. These types of dislocations are linked to the curvature of the grains, which is influenced by the manufacturing process, whether through plastic deformation or the extreme additive manufacturing conditions, where significant residual stresses coming from high cooling rates and repetitive fusion between adjacent layers are present [35–37]. In this context, two behaviors are observed following the various

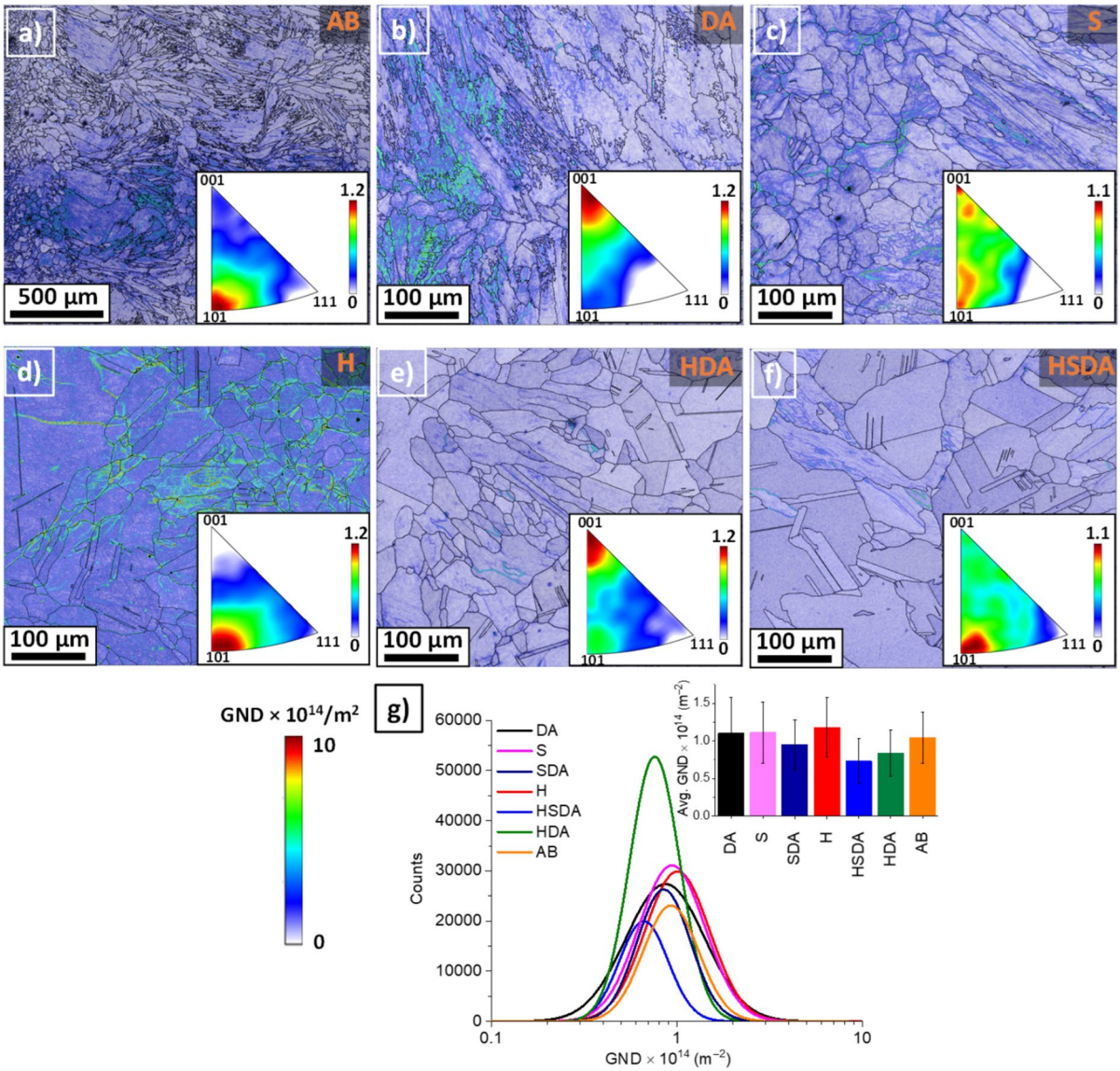

Fig. 7 Geometrically necessary dislocations (GNDs) maps and the weighted Burgers vector (WBV) representation for the different analyzed conditions. **a** AB, **b** DA, **c** S, **d** H, **e** HDA, **f** HSDA, and **g** GND distributions

HTs: first, HTs involving a single stage do not impact the GNDs magnitude compared to the as-built condition (see Figs. 7a-d). In contrast, HTs that include multiple thermal cycles reduce the magnitude of dislocations (see Fig. 7e-g). The significant decrease in GNDs observed in the SDA, HDA, and HSDA conditions aligns well with the previously described microstructural changes, where grain size and grain boundary misorientations underwent substantial alterations due to temperature-induced recrystallization.

Analysis of the dislocation orientations using the weighted Burgers vector triangle reveals a primary alignment between the $<001>$ and $<101>$ crystallographic directions. This observation is consistent with Nickel's Face-Centered Cubic (FCC) structure, for which the predominant slip systems are of the $\{111\}<110>$ type. Thus, most dislocations correspond to the $\frac{1}{2}[101]$ type, as observed in the as-built and homogenized conditions. However, different HTs show a more significant variability in dislocation orientations. This scattering can be attributed to the formation of second phases, such as precipitates or carbides, which generate dislocation tangles and distortions in the lattice.

Figure 8 presents the XRD spectra of both as-built and HT samples. In Fig. 8, two distinct phases—γ and δ—are identified, along with fluorescence peaks attributed to W, In, and Pb emissions, likely originating from the shielding walls and devices within the synchrotron hutch. Notably, only the H and S heat treatments resulted in a single-phase structure, whereas the as-built condition and all other heat-treatment

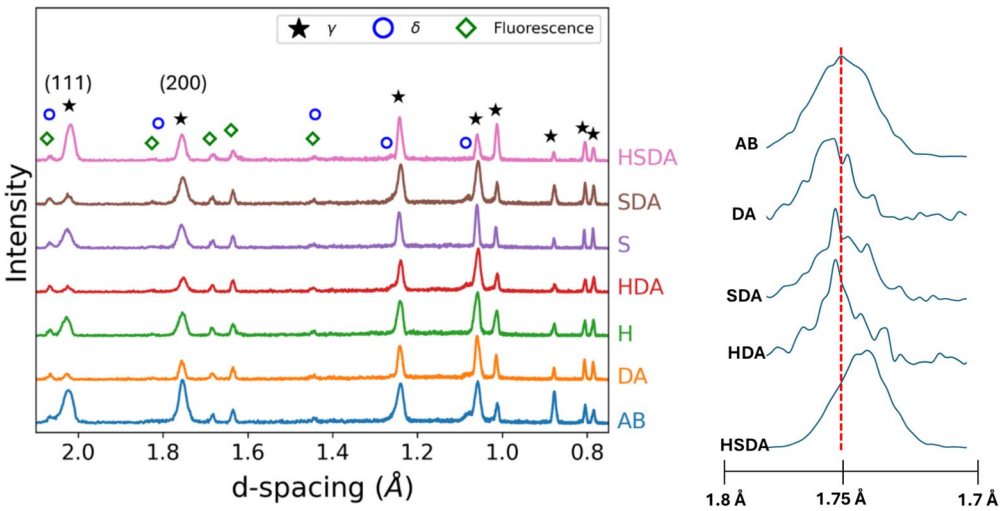

Fig. 8 Energy-dispersive X-ray diffraction pattern of the IN718 fabricated via DED in the as-built and heat-treated conditions, along with an in-depth view of the {200}γ peak

combinations led to the formation of the δ phase. It should be noted that the XRD analysis could not detect the presence of γ' and γ" phases, which is already expected due to their expected low volume fraction, which ranges from less than 1% to approximately 11%, depending on the employed HT conditions [38], small size, coherence with the matrix, and superimposition of diffraction peaks [39].

The as-built IN718 sample exhibited a higher relative intensity for the {200}γ peak than the {111}γ peak. This phenomenon is associated with the preferential growth along the <001> orientation, which is influenced by the significant thermal gradient present along the build direction [40, 41]. The XRD patterns of the HT samples revealed subtle differences among {111}γ and {200}γ peaks. Additionally, minor peaks were observed between the {111}γ and {200}γ peaks, indicating the formation of the δ-phase [42, 43]. In contrast, the HSDA sample exhibited a {111}γ peak with higher intensity than the {200}γ peak, probably due to the grain growth or recrystallization during the HT at 1100 °C [44]. Furthermore, the XRD spectra of the DA samples suggest the development of a more random orientation, akin to that observed in the Mackenzie curve from Fig. 4c. Moreover, the XRD spectrum of the other HT samples also suggests a more randomized crystallographic orientation, as the relative intensity of matrix peaks follows the calculated values.

Detailed diffraction patterns in the vicinity of the {200} γ peaks for all samples are also presented in Fig. 8. The evolution of the γ{200} peak with the complexity of the HT, i.e., following the sequence of conditions: as-built → DA → SDA → HDA → HSDA, is almost none, indicated by the dashed red line, except the HSDA HT, which shifts to a lower interplanar spacing. This indicates a reduction in the lattice parameter of the γ matrix. This shift is primarily attributed to the precipitation of the γ″ phase, which reduces the concentration of dissolved Nb in the γ matrix. However, distinguishing their contributions in the XRD pattern proved challenging due to the issues already mentioned [45].

Figure 9 shows thermodynamic calculations considering either the non-equilibrium (Scheil–Gulliver, a) or the thermodynamic equilibrium (phase diagram, b) for IN718 alloy. δ, γ', γ" were considered one phase in the calculations due to their similar chemical composition, and they are called Ni_3(Nb, Ti). The solidification path predicted for the present composition of IN718 alloy is as follows:

$$\begin{aligned} &Liquid\,(L) \rightarrow L + \gamma \rightarrow L + \gamma + NbC \\ &\rightarrow L + \gamma + NbC + Laves + Ni_3(Nb, Ti) \\ &\rightarrow L + \gamma + NbC + Laves + Ni_3(Nb, Ti) + \sigma. \end{aligned}$$

The non-equilibrium thermodynamic conditions inherent to additive manufacturing promote the formation of metastable phases. The Scheil–Gulliver solidification model accurately predicts transition temperatures, revealing Laves phase formation between 1180 and 1185 °C. Below 1180 °C, chemical element stoichiometry enables Ni_3Nb phase development. Microsegregation introduces complexity, with low-solubility elements like Nb, Mo, Ti, and C concentrating in interdendritic regions and forming MC carbides and Laves phases. This segregation can induce variations in precipitation temperatures, highlighting the intricate microstructural evolution during DED processing.

On the other hand, phase equilibrium calculations show an insignificant presence of NbC, besides a considerable

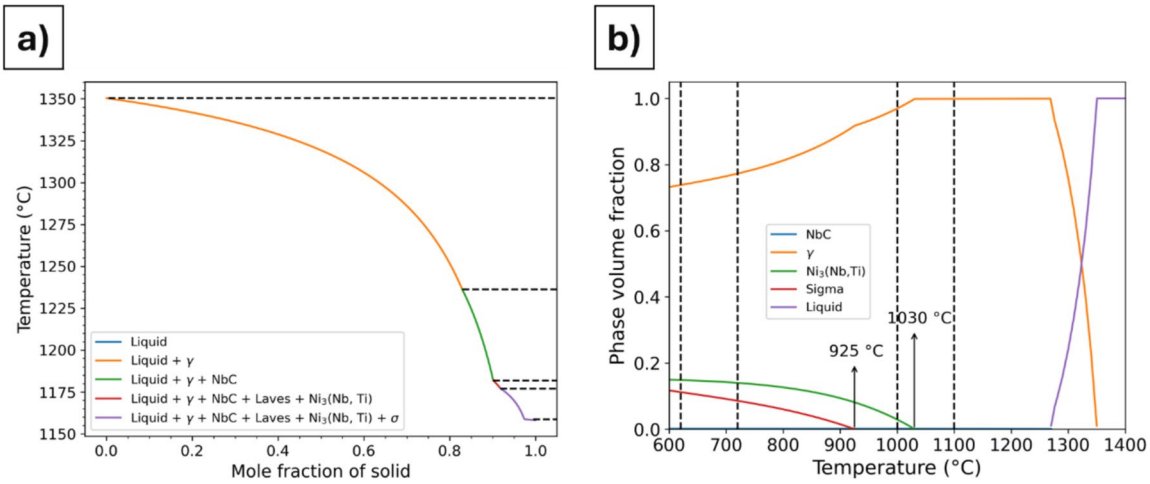

Fig. 9 **a** Solidification path of IN718 alloy, predicted by Thermo-Calc software using Scheil–Gulliver solidification mode; **b** phase volume fraction of the DED IN718 phases

presence of σ phase at low temperature, which continues to dissolve until 925 °C, and Ni_3(Nb, Ti), achieving its complete dissolution at 1030 °C. The phase equilibrium calculation at each heat-treatment temperature condition is depicted in Table 1.

Table 1 Phase volume percent at heat-treatment temperatures under equilibrium conditions.

Temperature (°C)	Phases (vol.%)			
	NbC	γ	Ni_3(Nb,Ti)	σ
620	0.1	73.8	14.8	11.2
720	0.1	77.3	14.0	8.6
1000	0.1	96.9	2.9	-
1100	0.1	99.9	-	-

Intermetallic phase formation in DED manufacturing of IN718 alloy emerges from complex interactions between kinetic processes, thermal history, and elemental availability. The alloy demonstrates coexistence of stable (δ) and metastable (γ″) phases with Ni_3Nb stoichiometry, with phase prevalence critically dependent on temperature gradients and elemental distribution [38, 46]. Temperatures exceeding 600 °C trigger MC carbide precipitation, predominantly NbC, with carbide growth dependent upon Nb concentration in δ and γ″ phases. The metastable γ″ phase is the primary strengthening precipitate, significantly enhancing mechanical properties. However, prolonged high-temperature exposure induces transformation to the stable δ phase, potentially compromising material strength [38, 46].

Figure 10 shows the SEM and EDS analysis for all the aged samples. Microstructural comparisons of as-built and DA samples revealed minimal morphological distinctions through SEM micrographic analysis. Characteristic precipitates, specifically Laves phase, were consistently observed in both conditions, suggesting that the applied aging temperatures were insufficient to induce complete dissolution of the Laves phase (Fig. 10a). Figure 10b depicts the SDA sample microstructure, showing that the cellular microstructure persisted. It can be seen that localized grain growth occurs compared to the as-built condition. From the EDS analysis, shown as a table on the side of the micrographs, the possible identification of those phases as δ precipitates and carbides can be seen. Homogenization treatments, namely HDA and HSDA, Fig. 10c and d, respectively, effectively eliminated melt pool boundaries and elemental segregation. Significant microstructural transformations were observed, including extensive recrystallization and grain growth, with grain sizes exceeding 200 µm in a bimodal fashion, as shown in Fig. 6. Annealing twins were detected, and grain boundaries exhibited small white particles (Fig. 10c), tentatively identified as carbides; Fig. 10d also shows the presence of carbides and possibly δ precipitates inside the grains.

3.2 Mechanical properties

Hardness test results for the DED and the forged materials are shown in Fig. 11. The DA heat treatment enhanced the material's mechanical strength by approximately 50% compared to non-aged samples, reaching average values of 475.7 HV, 503.5 HV, 506.1 HV, and 483.5 HV for DA, HDA, SDA, and HSDA, respectively. The authors believe that it occurs due to the precipitation of the strengthening phases of the IN718 alloy, i.e., γ' and γ'', which could not be detected by the XRD analysis. Furthermore, it can be noticed that the

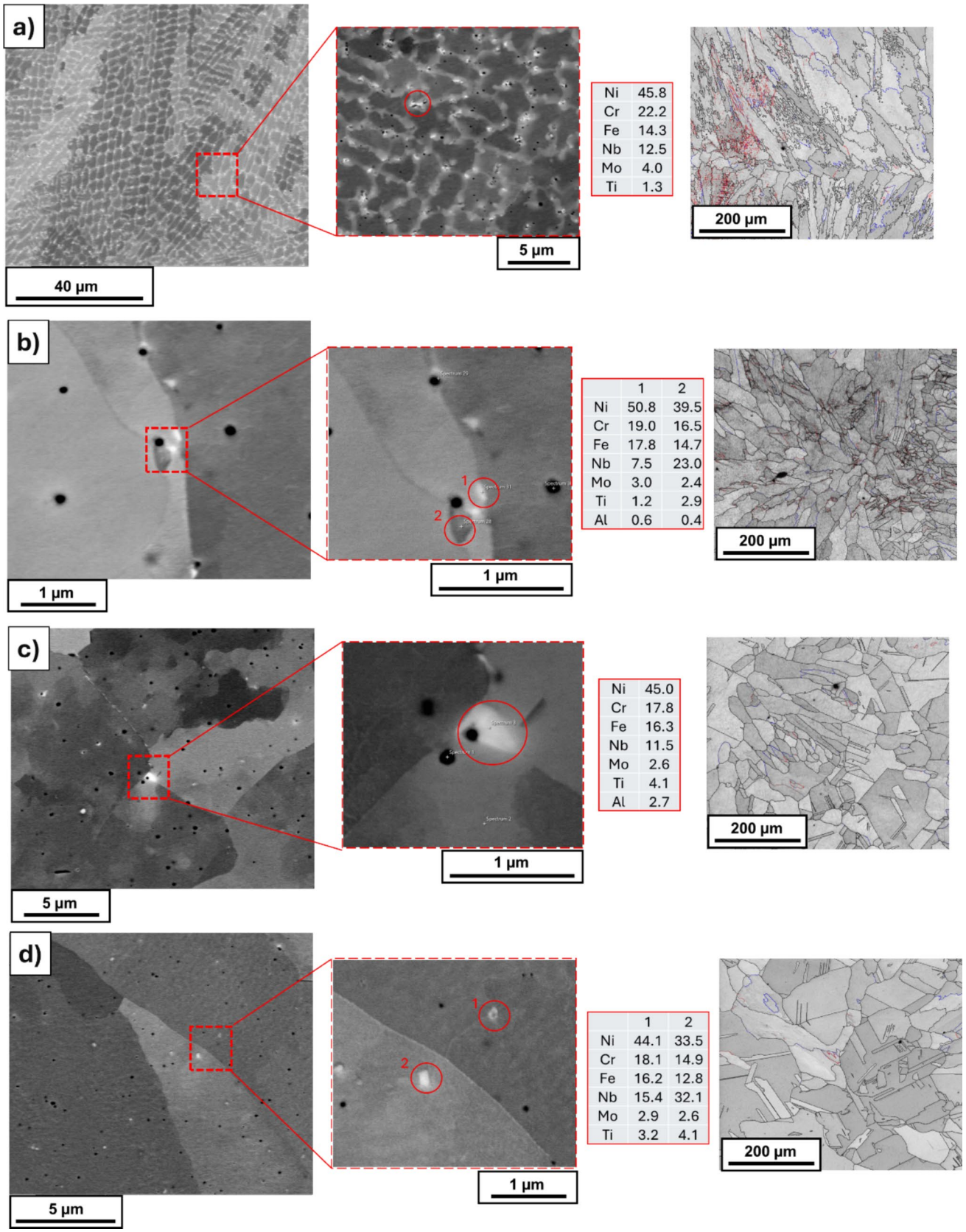

Fig. 10 Scanning electron microscopy images, EDS measurements, and EBSD band contrast maps with HAGB as black lines for **a** DA, **b** SDA, **c** HDA, and **d** HSDA HT conditions

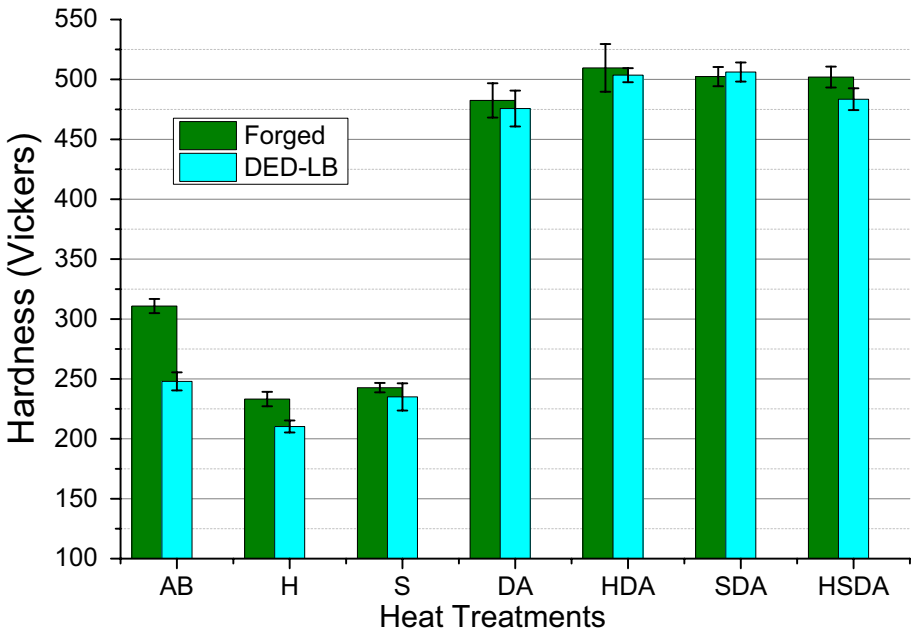

Fig. 11 Vickers hardness results for the AB, forged, and HT conditions

H and S heat treatments could solubilize the alloy, reducing its hardness values. While forged materials typically exhibit higher hardness than their AM counterparts—a result of the grain refinement and increased dislocation density induced by severe plastic deformation—this study demonstrates that optimized HTs can effectively bridge this performance gap. Following the selected aging treatments, the DED samples achieved hardness values comparable to the forged IN718 reference material. This highlights the critical role of post-processing in unlocking the mechanical potential of DED components, enabling them to reach a performance level equivalent to that of conventionally processed materials [47]. In contrast, AM processes often result in columnar and dendritic microstructures with lower dislocation density due to rapid solidification and lack of plastic deformation. Additionally, AM components tend to exhibit higher porosity and process-induced defects, reducing mechanical performance compared to the dense and homogeneous microstructure of forged materials [48].

Residual compressive stresses in forged materials further contribute to their superior hardness, whereas AM components often require post-processing HTs to mitigate tensile residual stresses and improve mechanical properties [48]. While AM advancements are narrowing this gap, forged materials generally maintain superior hardness due to their refined microstructure and defect-free nature.

Figure 12a presents the engineering stress–strain curves for all analyzed conditions. Upon initial observation, there is a wide range of combinations of strength and ductility, with yield strengths varying from 300 to 1200 MPa and fracture strains ranging from 0.5 to 0.35. Single-stage HTs, such as homogenization and solubilization, resulted in the highest ductility. In contrast, thermal cycles that involve aging HTs, such as DA, SDA, HDA, and HSDA, yield greater strengths than the as-built condition.

The strain-hardening rate curves demonstrate that ductility is enhanced following the S and H heat treatments. In contrast, the aged conditions exhibit reduced ductility, which leads to localized plastic instability during early deformations, as shown in Fig. 12b. This loss of ductility in the aged conditions can be attributed to the large number of precipitates at the grain boundaries, as confirmed in Fig. 10. The formation of precipitates at grain boundaries can increase brittleness, particularly when the particles are incoherent and large. Studies have shown that the coarsening of γ' precipitates after HT follows the Ostwald ripening mechanism. This process results in a loss of ductility due to strain concentration caused by the incoherent precipitates localized at the grain boundaries [49, 50].

The strain profiles observed during tensile tests at various deformations reveal different behaviors depending on the applied HT. After the HDA HT, the strain distribution along the calibrated length shows significant heterogeneity from the start until the onset of plastic instability (see Fig. 12c). In the as-built condition, the strain profiles exhibit multiple peaks, which indicate strain localization at different points along the sample length, thereby delaying the formation of plastic instability (see Fig. 12d). In contrast, the homogenized condition displays strain profiles with less heterogeneity than the ones mentioned earlier. These profiles resemble a plateau, facilitating the storage of larger and more uniform deformations before the plastic instability (Fig. 12e). The behaviors discussed are closely related to the various microstructures described. For instance, the early

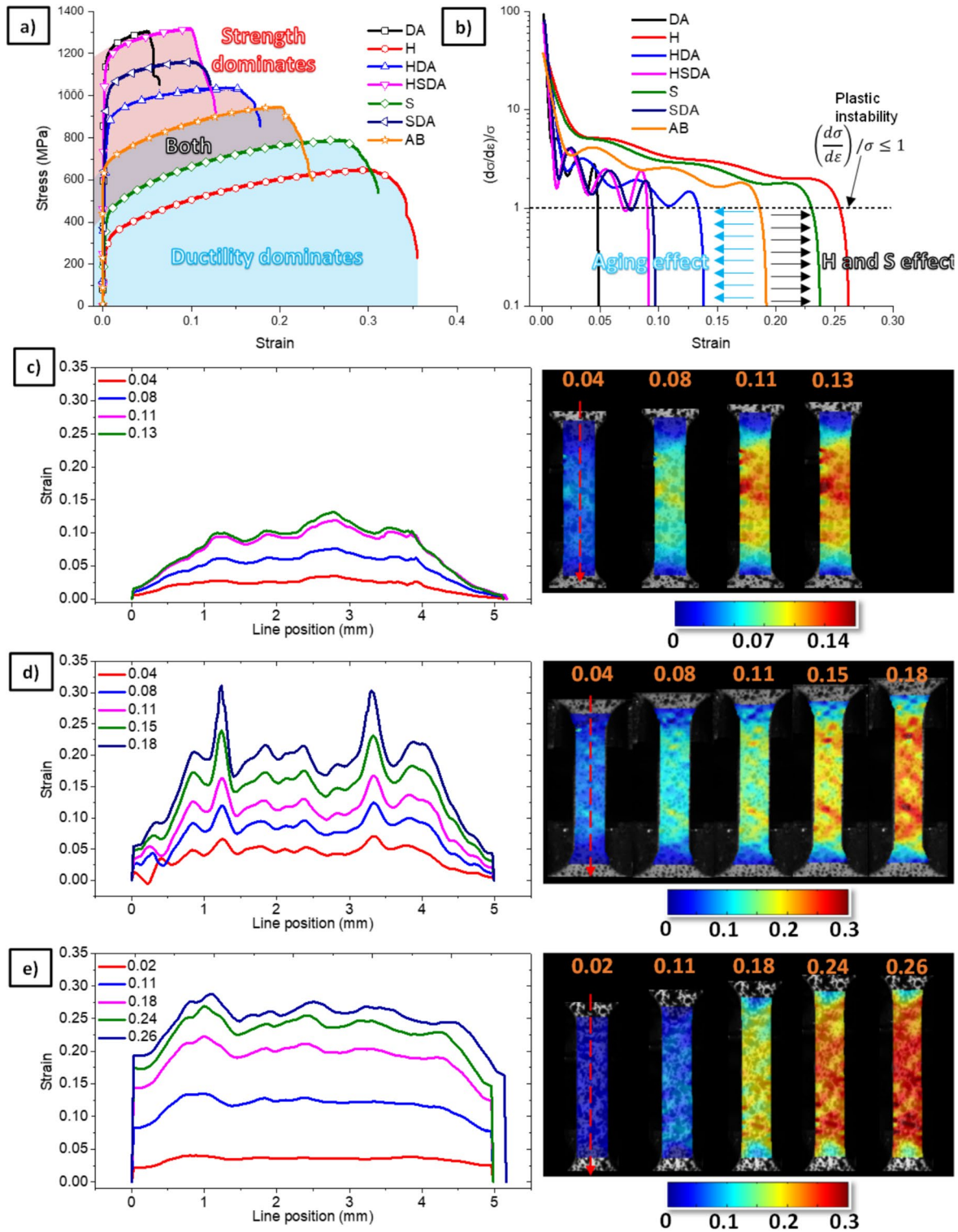

Fig. 12 **a** Engineering stress–strain curves for all HT conditions, **b** strain-hardening rate curves for all HT conditions, **c** strain hardening of the HDA condition, **d** strain hardening of the AB condition, and **e** strain hardening of the H condition.

onset of strain localization in the HDA can be attributed to the brittleness caused by the coarse precipitates at the grain boundaries. In contrast, the multiple peaks observed in the as-built condition can be linked to the residual stresses arising from the manufacturing process, which are repeated between adjacent melt pools. In the homogenized condition,

the more uniform strain distribution is due to the absence of precipitates and the larger, more equiaxed grain size resulting from the recrystallized microstructure, which allows for greater dislocation motion.

Therefore, a positive synergy between strength and ductility in the studied alloy is probably achieved by an adequate distribution of coherent and intragranular γ'/ γ'' precipitates, which impart strength while controlling the number of precipitates at the grain boundaries to avoid ductility loss.

Figure 13 presents the room-temperature mechanical properties of the DED processed IN718 alloy in both the as-built state and after six distinct HT conditions. The average yield strength values for the as-built, DA, H, S, HDA, SDA, and HSDA conditions were determined to be approximately 638 MPa, 1195 MPa, 360 MPa, 412 MPa, 1037 MPa, 1189 MPa, and 1046 MPa, respectively. Additionally, the average elongation values for these conditions were measured as ≈28.5%, 8.0%, 49.3%, 47.1%, 17.8%, 12.1%, and 16.7%, respectively. To characterize the plastic deformation behavior observed during tensile testing, the Hollomon equation ($\sigma = K \cdot \varepsilon^n$, where σ represents the true stress, K is the strength coefficient, ε denotes the true strain, and n is the strain-hardening exponent) was employed. The calculated n values for the DA, H, S, HDA, SDA, and HSDA samples were approximately 0.072, 0.281, 0.25, 0.085, 0.06, and 0.082, respectively. These results indicate that the H and S conditions exhibit the highest uniform plastic deformation capacity, whereas the aged conditions display increased hardness and reduced deformability. The average elastic modulus (E) values were determined to be ≈ 203 GPa for the as-built sample, 211 GPa, 197 GPa, 203 GPa, 214 GPa, 210 GPa, and 220 GPa for the DA, H, S, HDA, SDA, and HSDA conditions, respectively. This suggests that the HSDA sample demonstrates the greatest resistance to elastic deformation.

The presence of γ'/γ" strengthening phases, which develop during the DA process, contributes to an increase in tensile strength, explaining why the homogenized and solubilized conditions, lacking these phases, exhibit comparatively lower strength. Among the evaluated HT conditions, DA results in the highest tensile strength; however, it also leads to the lowest ductility. In contrast, solution annealing provides slightly higher tensile strength than homogenization solution aging, though at the cost of reduced ductility, while maintaining comparable overall tensile properties [51].

4 Conclusions

This study systematically investigated the influence of six distinct post-processing HT strategies on the microstructural evolution and mechanical properties of IN718 fabricated by DED. The findings demonstrate that HTs are a critical tool for tailoring the material's performance, enabling a broad range of properties suitable for different demands. The primary conclusions are as follows:

1. The AB DED microstructure, characterized by columnar dendritic grains, high dislocation density, and the presence of deleterious Laves phase, was significantly altered by the applied HTs. Homogenization treatments (H, HDA, and HSDA) proved most effective at modifying the initial microstructure, inducing recrystallization that replaced the columnar morphology with more equiaxed grains and annealing twins. In contrast, solubili-

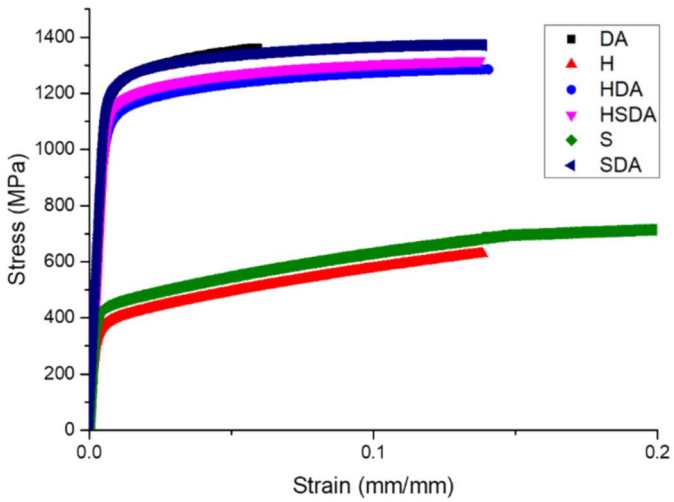

	DA	S	H	SDA	HDA	HSDA
UTS (MPa)	1366 ± 3	825 ± 1	796 ± 1	1363 ± 21	1306 ± 8	1320 ± 11
YS (MPa)	1214 ± 19	447 ± 37	355 ± 6	1236 ± 48	1063 ± 26	1079 ± 33
ELF (%)	8.0 ± 4.0	47.1 ± 2.0	49.3 ± 0.1	12.1 ± 0.9	17.8 ± 0.2	16.7 ± 2.0
E (GPa)	204 ± 2	202 ± 2	210 ± 2	216 ± 6	215 ± 1	235 ± 15

Fig. 13 Tensile test results for the heat-treated DED IN718 samples. Results are shown only until the contact strain gauge was removed

zation and direct aging treatments (S, DA, and SDA) largely retained the AB grain structure.

2. These experimental findings were further supported by thermodynamic modeling, which provided a theoretical basis for the observed phase transformations. The non-equilibrium Scheil–Gulliver model, which emulates the rapid solidification conditions of DED, accurately predicted the formation of the Laves phase due to microsegregation in interdendritic regions. Meanwhile, equilibrium calculations clarified the dissolution temperatures of key phases, such as $Ni_3(Nb, Ti)$ at 1030 °C, aligning with the microstructural changes observed after the homogenization treatment.
3. A clear trade-off between strength and ductility was established, directly correlating with the microstructural changes. Aging cycles (DA, SDA, HDA, and HSDA) probably prompted the precipitation of γ'/γ'' strengthening phases, leading to a substantial increase in hardness (up to 506 HV) and yield strength (up to 1195 MPa). However, this came at the cost of reduced ductility, particularly in the DA and SDA conditions, where elongation fell to as low as 8.0% and 12.1%, respectively.
4. Conversely, heat treatments without a final aging step (H and S) resulted in superior ductility, with elongation values approaching 50%. This was attributed to the dissolution of strength-reducing phases like Laves and the formation of a more uniform, recrystallized microstructure free from strengthening precipitates. These conditions facilitated more homogeneous strain distribution and delayed the onset of plastic instability.
5. The combined homogenization and aging treatments (HDA and HSDA) offered the most balanced mechanical response. These routes successfully dissolved the detrimental as-built phases and refined the grain structure through recrystallization, while still achieving high strength through subsequent aging. The resulting properties—a yield strength exceeding 1000 MPa coupled with elongations of approximately 17%—demonstrate a possible path to producing DED IN718 components with a combination of strength and toughness that rivals conventionally processed counterparts.

Ultimately, this work provides a detailed framework for selecting an appropriate HT pathway based on the desired final application. Whether the priority is maximizing strength, ductility, or achieving a robust balance between the two, the specific post-processing route is the key to unlocking the full potential of additively manufactured IN718 components.

Acknowledgements The support of the Center for Research and Innovation in Materials and Structures (CEPIMATE) is deeply appreciated. This research used facilities of the Brazilian Nanotechnology National Laboratory (LNNano), part of the Brazilian Centre for Research in Energy and Materials (CNPEM), a private non-profit organization under the supervision of the Brazilian Ministry for Science, Technology, and Innovations (MCTI). The Electron Microscopy Laboratory staff is acknowledged for their assistance during the experiments (proposal SEM-FIB-C1-20233619). The authors acknowledge DESY (Hamburg, Germany), a member of the Helmholtz Association HGF, for providing the experimental facilities. Parts of this research were carried out at PETRA III (proposal I-20230101 EC), and they would like to thank Dr. Guilherme Abreu Faria and Dr. Marc-André Nielsen for their assistance in using beamline P61A.

Author contributions T. R. F. Cavalcante was responsible for writing the manuscript, editing the text, and preparing all figures. D. G. Bon conducted the mechanical testing and contributed to the analysis and interpretation of mechanical behavior. J. A. Muñoz performed the digital image correlation (DIC) analysis and contributed to data interpretation. G. G. Ribamar, J. P. Oliveira, and A. B. Pereira carried out the simulation work and participated in the X-ray diffraction (XRD) analysis. F. E. Mariani contributed to the experimental design and supervised the additive manufacturing process. J. C. Muñoz, R. T. Coelho and J. A. A. Diaz provided project supervision, critical review of the manuscript, and guidance throughout the research. All authors discussed the results, contributed to the final version of the manuscript, and approved its submission.

Funding This work was funded by Fundação de Amparo à Pesquisa do Estado de São Paulo—FAPESP, under Grant No. 2020/09079-2. This study was partly financed by the Conselho Nacional de Desenvolvimento Científico e Tecnológico—CNPq, under Grant No. 306960/2021–4. Thiago Roberto Felisardo Cavalcante recognizes the financial support through the Ph.D. scholarship from the Coordenação de Aperfeiçoamento de Pessoal de Nível Superior—Brasil (CAPES)—Finance Code 001 and CAPES PrInt, process 88887.886782/2023-00. JPO acknowledges funding by national funds from FCT—Fundação para a Ciência e a Tecnologia, I.P., in the scope of the projects LA/P/0037/2020, UIDP/50025/2020, and UIDB/50025/2020 of the Associate Laboratory Institute of Nanostructures, Nanomodelling and Nanofabrication—i3N. The present study was in part developed in the scope of the Project "Agenda ILLIANCE" [C644919832-00000035 | Project nº 46], financed by PRR—Plano de Recuperação e Resiliência under the Next Generation EU from the European Union.

Data availability The data supporting this study's findings are available from the corresponding author, J. A. Avila, upon reasonable request. No datasets were generated or analyzed during the current study.

Declarations

Conflict of interest The authors declare no competing interests.

References

1. Zhang W et al (2021) Effect of solution temperature on the microstructure and mechanical properties of Hastelloy X superalloy fabricated by laser directed energy deposition. Mater Sci Eng, A 820:141537. https://doi.org/10.1016/j.msea.2021.141537
2. Jiang R et al (2020) Effect of heat treatment on microstructural evolution and hardness homogeneity in laser powder bed fusion of alloy 718. Addit Manuf 35:101282. https://doi.org/10.1016/j.addma.2020.101282
3. Raghavan S et al (2017) Effect of different heat treatments on the microstructure and mechanical properties in selective laser melted

INCONEL 718 alloy. Mater Manuf Processes 32(14):1588–1595. https://doi.org/10.1080/10426914.2016.1257805
4. Zhao Y et al (2020) The effect of subsequent heat treatment on the evolution behavior of second phase particles and mechanical properties of the Inconel 718 superalloy manufactured by selective laser melting. Mater Sci Eng, A 794:139931. https://doi.org/10.1016/j.msea.2020.139931
5. Donachie MJ, Stephen J (2002) Donachie, Superalloys: a technical guide. ASM International
6. Collier JP, Wong SH, Tien JK, Phillips JC (1988) The effect of varying AI, Ti,and Nb content on the phase stability of INCONEL 718. Metall Trans A 19(7):1657–1666. https://doi.org/10.1007/BF02645133
7. Burad P, Gullipalli C, Thawari N, Gupta TVK (2023) Direct laser-deposited IN718 alloy: effect of heat treatment route on microstructural evolution and mechanical properties. J Mater Eng Perform 32(19):8961–8971. https://doi.org/10.1007/s11665-022-07744-x
8. Sui S, Chen J, Li Z, Li H, Zhao X, Tan H (2020) Investigation of dissolution behavior of laves phase in inconel 718 fabricated by laser directed energy deposition. Addit Manuf 32:101055. https://doi.org/10.1016/j.addma.2020.101055
9. Chen Y et al (2019) Study on the element segregation and Laves phase formation in the laser metal deposited IN718 superalloy by flat top laser and gaussian distribution laser. Mater Sci Eng, A 754:339–347. https://doi.org/10.1016/j.msea.2019.03.096
10. Xu L, Chai Z, Peng B, Zhou W, Chen X (2023) Effect of heat treatment on microstructures and mechanical properties of Inconel 718 additively manufactured using gradient laser power. Mater Sci Eng A 868(December 2022):144754. https://doi.org/10.1016/j.msea.2023.144754
11. Radavich JL (1989) Superalloys 718 – metallurgy and applications,1st ed., vol 1. TMS, Warrendale, PA
12. Qi H, Azer M, Ritter A (2009) Studies of standard heat treatment effects on microstructure and mechanical properties of laser net shape manufactured INCONEL 718. Metall and Mater Trans A 40(10):2410–2422. https://doi.org/10.1007/s11661-009-9949-3
13. Huang W, Yang J, Yang H, Jing G, Wang Z, Zeng X (2019) Heat treatment of Inconel 718 produced by selective laser melting: Microstructure and mechanical properties. Mater Sci Eng, A 750:98–107. https://doi.org/10.1016/j.msea.2019.02.046
14. Zhai Y, Lados DA, Brown EJ, Vigilante GN (2019) Understanding the microstructure and mechanical properties of Ti-6Al-4V and Inconel 718 alloys manufactured by laser engineered net shaping. Addit Manuf 27:334–344. https://doi.org/10.1016/j.addma.2019.02.017
15. Zhao Y, Meng F, Liu C, Tan S, Xiong W (2021) Impact of homogenization on microstructure-property relationships of Inconel 718 alloy prepared by laser powder bed fusion. Mater Sci Eng, A 826:141973. https://doi.org/10.1016/j.msea.2021.141973
16. Sui S et al (2021) Laves phase tuning for enhancing high temperature mechanical property improvement in laser directed energy deposited Inconel 718. Compos B Eng 215:108819. https://doi.org/10.1016/j.compositesb.2021.108819
17. Yu X et al (2020) Influence of post-heat-treatment on the microstructure and fracture toughness properties of Inconel 718 fabricated with laser directed energy deposition additive manufacturing. Mater Sci Eng A 798:140092. https://doi.org/10.1016/j.msea.2020.140092
18. Jang J, Van D, Lee SH (2022) Precipitation kinetics of secondary phases induced by heat accumulation in the deposit of Inconel 718. Addit Manuf. https://doi.org/10.1016/j.addma.2022.102831
19. Cavalcante TRF et al (2025) As-built microstructure and mechanical behavior of Inconel 718 processed via directed energy deposition with laser beam. Progress Additive Manuf. https://doi.org/10.1007/s40964-025-01054-z
20. ASTM INTERNATIONAL, "ASTM E384–22 Standard Test Method for Microindentation Hardness of Materials," 2022, https://doi.org/10.1520/E0384.
21. Wheeler J, Mariani E, Piazolo S, Prior DJ, Trimby P, Drury MR (2009) The weighted burgers vector: a new quantity for constraining dislocation densities and types using electron backscatter diffraction on 2D sections through crystalline materials. J Microsc 233(3):482–494. https://doi.org/10.1111/j.1365-2818.2009.03136.x
22. Blaber J, Adair B, Antoniou A (2015) Ncorr: open-source 2D digital image correlation Matlab software. Exp Mech 55(6):1105–1122. https://doi.org/10.1007/s11340-015-0009-1
23. *ASTM E8 / E8M-16ae1, Standard Test Methods for Tension Testing of Metallic Materials*. West Conshohocken, PA: ASTM International, 2016. https://doi.org/10.1520/E0008_E0008M-16AE01.
24. Dass A, Moridi A (2019) State of the art in directed energy deposition: from additive manufacturing to materials design. Coatings 9(7):418. https://doi.org/10.3390/coatings9070418
25. Hosseini E, Popovich VA (2019) A review of mechanical properties of additively manufactured Inconel 718. Additive Manuf. https://doi.org/10.1016/j.addma.2019.100877
26. Choudhary S, Pandey A, Gaur V (2023) Role of microstructural phases in enhanced mechanical properties of additively manufactured IN718 alloy. Mater Sci Eng, A 862:144484. https://doi.org/10.1016/j.msea.2022.144484
27. Park S, Tanaka Y, Okazaki S, Funakoshi Y, Kawashima H, Matsunaga H (2023) "Inferior fatigue resistance of additively-manufactured Ni-based superalloy 718 and its dominating factor. Int J Fatigue. https://doi.org/10.1016/j.ijfatigue.2023.107801
28. Wang G et al (2020) The origin of high-density dislocations in additively manufactured metals. Mater Res Lett 8(8):283–290. https://doi.org/10.1080/21663831.2020.1751739
29. Muñoz JA, Elizalde S, Komissarov A, Cabrera JM (2022) Effect of heat treatments on the mechanical and microstructural behavior of a hypoeutectic Al alloy obtained by laser powder bed fusion. Mater Sci Eng, A 857:144091. https://doi.org/10.1016/j.msea.2022.144091
30. Humphreys FJ, Hatherly M (2004) Recrystallization and Related Annealing Phenomena. Elsevier
31. Huang W, Garmestani H, Liang SY (2025) Microstructure evolution and the influence on residual stress in metal additive manufacturing with analytics. Crystals (Basel) 15(5):435. https://doi.org/10.3390/cryst15050435
32. Hu YL et al (2018) Evolution of solidification microstructure and dynamic recrystallisation of Inconel 625 during laser solid forming process. J Mater Sci 53(22):15650–15666. https://doi.org/10.1007/s10853-018-2701-x
33. Fencheng L, Xin L, Weiwei Z, Xiaoming Z, Jing C, Weidong H (2010) Effects of solution treatment temperature on microstructures and properties of laser solid forming GH4169 superalloy. Rare Metal Mater Eng 39(9):1519–1524. https://doi.org/10.1016/S1875-5372(10)60122-1
34. Ren YM, Lin X, Fu X, Tan H, Chen J, Huang WD (2017) Microstructure and deformation behavior of Ti-6Al-4V alloy by high-power laser solid forming. Acta Mater 132:82–95. https://doi.org/10.1016/j.actamat.2017.04.026
35. Nye JF (1953) Some geometrical relations in dislocated crystals. Acta Metall 1(2):153–162. https://doi.org/10.1016/0001-6160(53)90054-6
36. Muñoz JA (2019) Geometrically Necessary Dislocations (GNDs) in iron processed by Equal Channel Angular Pressing (ECAP). Mater Lett 238:42–45. https://doi.org/10.1016/j.matlet.2018.11.142
37. Vaz RF, Avila JA, Barriobero-Vila P, Muñoz JA, Albaladejo V, Cano IG (2025) Heat treatment effect on microstructural evolution

of cold spray additive manufacturing Ti6Al4V. J Mater Sci 60(12):5558–5576. https://doi.org/10.1007/s10853-025-10760-6
38. Rielli VV, Theska F, Godor F, Stanojevic A, Oberwinkler B, Primig S (2021) Evolution of nanoscale precipitates during common Alloy 718 ageing treatments. Mater Des. https://doi.org/10.1016/j.matdes.2021.109762
39. Li RB, Yao M, Liu WC, He XC (2002) Isolation and determination for δ, γ′ and γ″ phases in Inconel 718 alloy. Scr Mater 46(9):635–638. https://doi.org/10.1016/S1359-6462(02)00041-6
40. Popovich VA, Borisov EV, Popovich AA, Sufiiarov VSh, Masaylo DV, Alzina L (2017) Functionally graded Inconel 718 processed by additive manufacturing: crystallographic texture, anisotropy of microstructure and mechanical properties. Mater Des 114:441–449. https://doi.org/10.1016/j.matdes.2016.10.075
41. Geiger F, Kunze K, Etter T (2016) Tailoring the texture of IN738LC processed by selective laser melting (SLM) by specific scanning strategies. Mater Sci Eng, A 661:240–246. https://doi.org/10.1016/j.msea.2016.03.036
42. Lass EA, Stoudt MR, Katz MB, Williams ME (2018) Precipitation and dissolution of δ and γ″ during heat treatment of a laser powder-bed fusion produced Ni-based superalloy. Scr Mater 154:83–86. https://doi.org/10.1016/j.scriptamat.2018.05.025
43. Stoudt MR et al (2018) The influence of annealing temperature and time on the formation of δ-phase in additively-manufactured inconel 625. Metall and Mater Trans A 49(7):3028–3037. https://doi.org/10.1007/s11661-018-4643-y
44. Amato KN et al (2012) Microstructures and mechanical behavior of Inconel 718 fabricated by selective laser melting. Acta Mater 60(5):2229–2239. https://doi.org/10.1016/j.actamat.2011.12.032
45. Zhou L, Mehta A, McWilliams B, Cho K, Sohn Y (2019) Microstructure, precipitates and mechanical properties of powder bed fused inconel 718 before and after heat treatment. J Mater Sci Technol 35(6):1153–1164. https://doi.org/10.1016/j.jmst.2018.12.006
46. Rielli VV, Piglione A, Pham MS, Primig S (2022) On the detailed morphological and chemical evolution of phases during laser powder bed fusion and common post-processing heat treatments of IN718. Addit Manuf 50:102540. https://doi.org/10.1016/j.addma.2021.102540
47. Hansen N (2004) Hall–Petch relation and boundary strengthening. Scr Mater 51(8):801–806. https://doi.org/10.1016/j.scriptamat.2004.06.002
48. Debroy T et al (2018) Additive manufacturing of metallic components – Process, structure and properties. Prog Mater Sci 92:112–224. https://doi.org/10.1016/j.pmatsci.2017.10.001
49. Zhang Y, Lan L, Zhao Y (2023) Effect of precipitated phases on the mechanical properties and fracture mechanisms of Inconel 718 alloy. Mater Sci Eng, A 864:144598. https://doi.org/10.1016/j.msea.2023.144598
50. Tucho WM et al (2024) Effects of δ phase and annealing twins on mechanical properties and impact toughness of L-PBF Inconel 718. J Manuf Mater Process. https://doi.org/10.3390/jmmp8040135
51. Deng D, Peng RL, Brodin H, Moverare J (2018) Microstructure and mechanical properties of Inconel 718 produced by selective laser melting: Sample orientation dependence and effects of post heat treatments. Mater Sci Eng, A 713:294–306. https://doi.org/10.1016/j.msea.2017.12.043

Authors and Affiliations

Thiago Roberto Felisardo Cavalcante[1] · Douglas Giovanni Bon[1] · Fábio Edson Mariani[1] · Reginaldo Teixeira Coelho[1] · Jairo Alberto Muñoz[2] · Jessica Calvo Muñoz[2] · Giovani Gonçalves Ribamar[3,4] · João Pedro Oliveira[3] · António Manuel de Bastos Pereira[4] · Julian Arnaldo Avila Diaz[5]

✉ Thiago Roberto Felisardo Cavalcante
thiagorfc@usp.br

✉ Julian Arnaldo Avila Diaz
julian.avila@unesp.br

Douglas Giovanni Bon
douglas.bon@usp.br

Fábio Edson Mariani
marianifabioe@gmail.com

Reginaldo Teixeira Coelho
rtcoelho@sc.usp.br

Jairo Alberto Muñoz
jairo.alberto.munoz@upc.edu

Jessica Calvo Muñoz
jessica.calvo@upc.edu

Giovani Gonçalves Ribamar
giovanigoncalvesr@gmail.com

João Pedro Oliveira
jp.oliveira@fct.unl.pt

António Manuel de Bastos Pereira
abastos@ua.pt

[1] Universidade de São Paulo, São Paulo, Brazil

[2] Universitat Politècnica de Catalunya, Barcelona, Spain

[3] Universidade Nova de Lisboa, Lisbon, Portugal

[4] University of Aveiro, Aveiro, Portugal

[5] São Paulo State University, São Paulo, Brazil